Chemical Science

ROYAL SOCIETY OF CHEMISTRY

EDGE ARTICLE

View Article Online
View Journal

Cite this: DOI: 10.1039/d5sc03850b

All publication charges for this article have been paid for by the Royal Society of Chemistry

Interfacial engineering of Ru–$RuSb_2$ for enhanced activity and stability towards alkaline hydrogen oxidation reaction†

Chaoyi Yang,‡ Zihao Dai,‡ Jianchao Yue and Wei Luo *

Although Ru has been regarded as the key candidate to replace Pt in alkaline hydrogen oxidation reaction (HOR), the substandard stability owing to its easy oxidation seriously impacts its practical application. In this work, we report the construction of a Ru–$RuSb_2$ heterostructure, showing excellent performance and stability towards alkaline HOR. Owing to the difference in the work functions of Ru and $RuSb_2$, the charge transfer induced by the build-in electric field modifies the electron distribution on the surface, enhancing the OH adsorption on the heterostructure. Moreover, the connectivity of the hydrogen bonding network is promoted with the inducing of OH species, which thereby leads to elevated proton transfer and accelerated HOR process, presenting a mass activity ($j^{k,m}$) of 2.098 mA μg^{-1} at 50 mV, which is 6-fold and 20-fold higher than those of Pt/C_{com} and Ru/NC, respectively. Owing to the change of the OH adsorption sites on Sb and the rapid HOR process on the surface, the pace of the oxidation on Ru of the heterostructure during the reaction largely slows down, contributing to the outstanding stability with only 2.59% decline in the activity.

Received 27th May 2025
Accepted 8th July 2025

DOI: 10.1039/d5sc03850b

rsc.li/chemical-science

Introduction

Hydrogen has been considered as the one of the most viable alternatives to the traditional fossil fuels owing to its high energy capacity, eco-friendliness and sustainability.[1–3] To efficiently utilize hydrogen, fuel cells have been regarded as the state-of-the-art hydrogen conversion devices.[4] Considering the utilization of non-precious metal catalysts for the cathodic oxygen reduction reaction in alkaline electrolytes, anion exchange membrane fuel cells (AEMFCs) have achieved great development in recent years.[5–7] However, the severe dependence on Pt catalysts and the sluggish kinetics in alkaline electrolytes for the anodic hydrogen oxidation reaction (HOR) substantially affect the performance of AEMFCs,[8–10] leading to the design of efficient non-Pt catalysts for alkaline HOR as the key for their practical application.

With similar properties and competitive price, ruthenium has been seen as the potential substitute for Pt catalysts for alkaline HOR.[11–13] The preference of OH species on Ru can promote the water formation step and thereby elevate the HOR performance.[14–16] The OH species on the surface can also regulate the interfacial water structure, promoting the connectivity of the hydrogen bonding network.[17] However, the strengthened adsorption of O-containing species such as OH may worsen the surface oxidation of Ru.[18,19] Its easy oxidation leads to activity degradation during long-time operation, largely affecting its long-time stability.[11–13] Therefore, enhancing the HOR activity and the stability of Ru catalysts at the same time is significant for their practical application in AEMFCs.

Herein, Ru–$RuSb_2$/NC has been synthesized and introduced as an efficient alkaline HOR catalyst. Owing to the construction of the heterostructure, the induced charge transfer between Ru and $RuSb_2$ redistributes the electrons on the surface, leading to enhanced OH adsorption on the Sb sites in Ru–$RuSb_2$/NC. The connectivity of the hydrogen bonding network on Ru–$RuSb_2$/NC is also enhanced with the strengthened OH adsorption, thus accelerating the HOR process and largely promoting the HOR activity. As a result, Ru–$RuSb_2$/NC presents an outstanding mass activity ($j^{k,m}$) of 2.098 mA μg^{-1} at 50 mV, which is 6-fold and 20-fold higher than that of Pt/C_{com} and Ru/NC, respectively. Due to the adsorption sites on Sb and the rapid reaction process, the oxidation of Ru during the reaction has been relieved and the HOR activity of Ru–$RuSb_2$/NC only decreases by 2.59% after the stability test.

Results and discussion

$RuSb_2$/NC was synthesized through high temperature calcination. Through the reduction of the addition of $SbCl_3$, the heterostructure of Ru–$RuSb_2$/NC was successfully obtained. As shown in Fig. 1a, both the hexagonal Ru phase (PDF #06-0667) and the orthorhombic $RuSb_2$ phase (PDF #71-0171) can be

College of Chemistry and Molecular Sciences, Wuhan University, Wuhan, Hubei 430072, P. R. China. E-mail: wluo@whu.edu.cn

† Electronic supplementary information (ESI) available. See DOI: https://doi.org/10.1039/d5sc03850b

‡ CY and ZD contributed equally to this work.

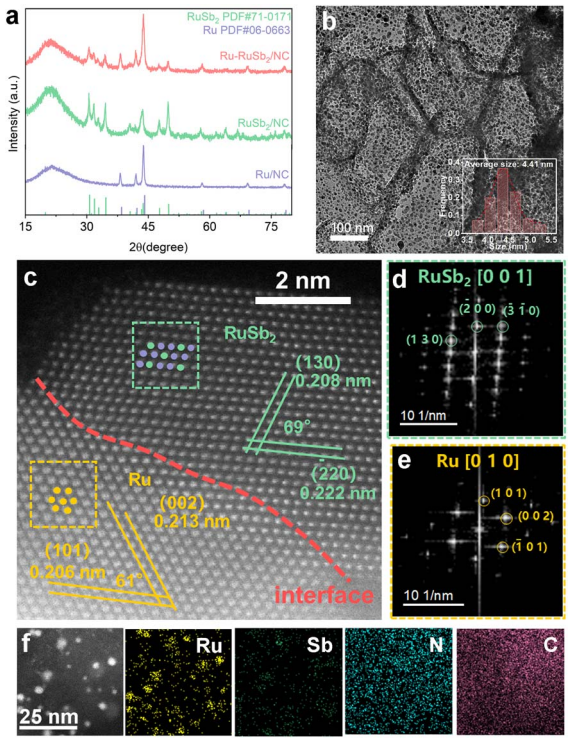

Fig. 1 (a) The XRD pattern of Ru/NC, Ru–$RuSb_2$/NC and $RuSb_2$/NC. (b) The TEM image of Ru–$RuSb_2$/NC and the corresponding size distribution. (c) The atomic-resolution HAADF-STEM image of Ru–$RuSb_2$/NC. The FFT of $RuSb_2$ (d) and Ru (e) from STEM images of panels (c). (f) HAADF STEM image and corresponding EDX mappings of Ru–$RuSb_2$/NC.

observed in the X-ray diffraction (XRD) pattern, indicating the formation of the heterostructures in Ru–$RuSb_2$/NC. The broad peak around 20° can be assigned to the substrate carbon. Besides, the counterparts Ru/NC and $RuSb_2$/NC were also synthesized for comparison and their XRD patterns in Fig. 1a matched well with the corresponding standard phase. Transmission electron microscopy (TEM) is employed to explore the morphology of the catalysts. As depicted in Fig. 1b, Ru–$RuSb_2$/NC consists of abundant nanoparticles with an average size of 4.41 nm evenly spread on the carbon substrate. The same morphology can also be observed in Ru/NC and $RuSb_2$/NC, presenting the similar average sizes of 4.46 nm and 4.39 nm, respectively (Fig. S1 and S2†). Through the high-angle annular dark-field scanning transmission electron microscopy (HAADF-STEM) image, the interface of Ru–$RuSb_2$/NC can be clearly observed in Fig. 1c. The lattice distances of 0.208 nm and 0.222 nm can be attributed to the (130) and ($\bar{2}$20) planes of $RuSb_2$, respectively, and the angle of the two planes is 69° which further confirms the $RuSb_2$ phase. Besides, the lattice fringes presented distances of 0.206 nm and 0.213 nm with the angle of 61°, which are assigned to the (101) and (002) planes of Ru, respectively. To better analyze the heterostructure, a fast Fourier transform (FFT) pattern of the green marked region and yellow marked region is shown in Fig. 1d and e, respectively. The presented characteristic crystal plane diffraction spots of (130), ($\bar{2}$20) and ($\bar{3}\bar{1}$0) in Fig. 1d imply the [001] crystallographic direction of $RuSb_2$. The diffraction spots attributed to the (101), (002) and ($\bar{1}$01) planes in Fig. 1e also confirm the [010] crystallographic direction of Ru, further verifying the formation of the heterostructure. Meanwhile, the energy-dispersive X-ray spectroscopy (EDX) mappings in Fig. 1f show that the Ru and Sb elements are homogeneously spread within the nanoparticle zone while the substrate is composed of the N and C elements.

X-ray photoelectron spectroscopy (XPS) was performed to explore the electron state in Ru–$RuSb_2$/NC. As shown in Fig. 2a, the peaks located around 460 eV and 482.5 eV can be assigned to the $3p_{3/2}$ and $3p_{1/2}$ of metallic Ru, respectively, while the peaks located at 463.5 eV and 485.5 eV correspond to the $3p_{3/2}$ and $3p_{1/2}$ of oxidized Ru, respectively.[20,21] The slight oxidation of Ru/NC may originate from the inevitable oxidation due to exposure to air. The binding energy of Ru in Ru–$RuSb_2$/NC is higher than that in Ru/NC and lower than that in $RuSb_2$/NC, indicating the electron transfer between Ru and $RuSb_2$. Fig. 2b depicts the Sb 3d spectra of $RuSb_2$/NC and Ru–$RuSb_2$/NC, which can be deconvoluted into two pairs of peaks located around 528.6 eV, 537.9 eV, 530.8 eV and 540.1 eV, belonging to the $3d_{5/2}$ and $3d_{3/2}$ of metallic Sb and the $3d_{5/2}$ and $3d_{3/2}$ of oxidized Sb.[22,23] The binding energy of Sb in Ru–$RuSb_2$/NC shifts to a higher position than that in $RuSb_2$/NC, implying the less electron acceptance from Ru in the heterostructure in line with the XPS results of Ru. Besides, the two peaks located around 530 eV and 531.5 eV can be attributed to the O_I and O_{II} states, which belong to the lattice oxygen in metal oxides and the hydroxy-like group, respectively.[23] To investigate the local coordination environment in the heterostructure, the X-ray absorption near edge structure (XANES) of both the Ru K-edge and Sb K-edge is tested. The normalized Ru K-edge XANES spectra of Ru–$RuSb_2$/NC and $RuSb_2$/NC are shown in Fig. 2c with Ru foil and RuO_2 as standards. The absorption edges of Ru–$RuSb_2$/NC and $RuSb_2$/NC are both positioned between those of Ru foil and RuO_2, implying the electron loss from Ru in the catalysts.[24,25] According to the scaling relationship between the valence state and absorption energy, the average valence of Ru in Ru–$RuSb_2$/NC is determined to be 1.41, lower than that in $RuSb_2$/CN (1.81), indicating the less average electron loss in the heterostructure (Fig. 2d).[26] The Fourier transforms of the Ru K-edge extended X-ray adsorption fine structure (EXAFS) spectra show that the only signal of Ru–$RuSb_2$/NC at 2.45 Å can be assigned to Ru–Ru/Sb (Fig. 2e). The fitting of the EXAFS results of Ru–$RuSb_2$/NC (Fig. 2f and g) shows that the Ru in the heterostructure is coordinated with average 10.88 Ru atoms and 3.88 Sb atoms. Compared with Ru ($CN_{Ru-Ru} = 12$) and $RuSb_2$ ($CN_{Ru-Sb} = 6$), the coordination numbers (CN) of Ru–Ru and Ru–Sb in Ru–$RuSb_2$/NC are both decreased, which further confirms the formation of the heterostructure.[27,28] Besides, the wavelet transforms (WT) for k^3-weighted EXAFS signals of the Ru K-edge depicted in Fig. 2h visualize the metallic properties of Ru in the heterostructure. Fig. S3a† shows the Sb K-edge XANES spectra of Ru–$RuSb_2$/NC and $RuSb_2$/NC. The spectra of Ru–$RuSb_2$/NC shift to higher energy than that of $RuSb_2$/NC, indicating the stronger electronic interaction owing to the formation of the heterostructure.[29] The EXAFS spectra of the Sb K edge

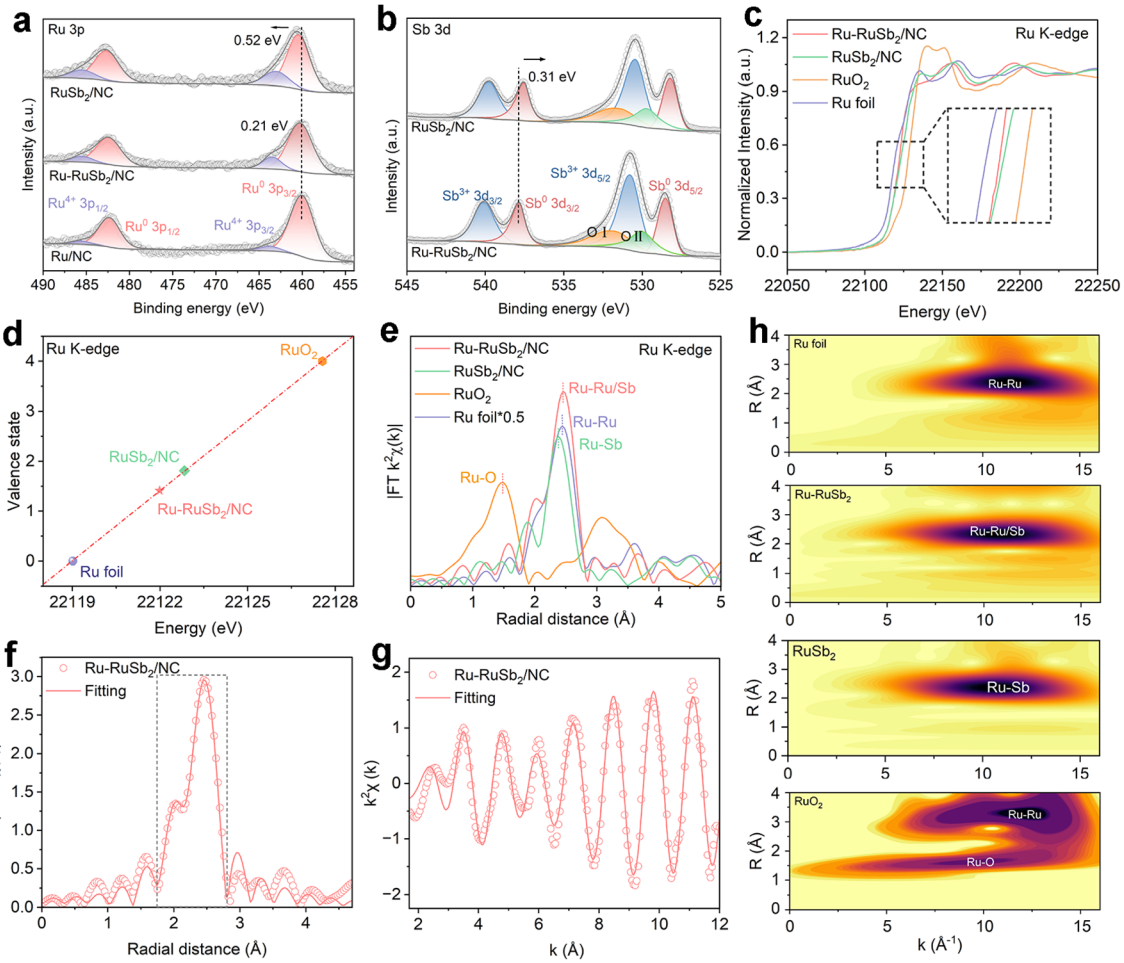

Fig. 2 (a) The Ru 3p XPS spectra of Ru/NC, Ru–$RuSb_2$/NC and $RuSb_2$/NC. (b) The Sb 3d XPS spectra of Ru–$RuSb_2$/NC and $RuSb_2$/NC. (c) Ru K-edge XANES spectra of Ru–$RuSb_2$/NC and $RuSb_2$/NC with reference to Ru foil and RuO_2. (d) The determination of Ru oxidation with reference samples of Ru foil and RuO_2. (e) Corresponding FT-EXAFS spectra of Ru–$RuSb_2$/NC and $RuSb_2$/NC with reference to Ru foil and RuO_2. (f) Ru K-edge EXAFS spectra fitting curve and (g) k^2-weighted EXAFS oscillations collected at the Ru K-edge of Ru–$RuSb_2$/NC. (h) Wavelet-transform (WT) for the EXAFS signals of Ru foil, Ru–$RuSb_2$/NC, $RuSb_2$/NC and RuO_2.

shown in Fig. S3b† present the Ru–Ru/Sb bond in Ru–$RuSb_2$/NC, excluding the formation of Sb–O in the heterostructure.

The HOR performance of Ru–$RuSb_2$/NC along with that of Ru/NC, $RuSb_2$/NC and Pt/C_{com} in H_2-saturated 0.1 M KOH electrolyte has been tested through a rotating disk electrode (RDE) with a rotating speed of 1600 rpm. Ru–$RuSb_2$/NC presents the highest exchange current density (j^0) of 2.39 mA cm^{-2} among all the catalysts, which is higher than that of Pt/C_{com} and $RuSb_2$/NC (Fig. 3a). The polarization curves with the rotating speed from 2500 to 400 rpm of all the samples have been tested and the corresponding linear relationships established between j^{-1} and $\omega^{-1/2}$ are depicted in Fig. S4–S7.† Through the Butler–Volmer fitting, the obtained Tafel plots of Ru/NC, $RuSb_2$/NC and Pt/C_{com} are shown in Fig. 3b, which presents the perfect kinetic current density (j^k) of 11.6 mA cm^{-2} at 50 mV for Ru–$RuSb_2$/NC.[30,31] The real PGM loading on the catalysts, obtained by inductively coupled plasma atomic emission spectroscopy (ICP-AES), is shown in Table S1.† Through the normalization of the j^k by the amount of noble metal, the mass activity ($j^{k,m}$) at 50 mV can be calculated as shown in Fig. 3c. Ru–$RuSb_2$/NC depicts the best mass activity ($j^{k,m}$) of 2.098 mA μg^{-1} at 50 mV, which is 6-fold and 20-fold higher than that of Pt/C_{com} and Ru/NC, respectively. To further compare the intrinsic activity ($j^{0,s}$) of the catalysts, Cu underpotential deposition (Cu-UPD) stripping was applied to examine the electrochemical active surface areas (ECSAs) (Fig. S8†).[32] The obtained intrinsic activities ($j^{0,s}$) which are normalized by the ECSA in Fig. 3c also present the excellent $j^{0,s}$ of 0.591 mA cm^{-2} for Ru–$RuSb_2$/NC, which is 2 times higher than that of Pt/C_{com} and 3 times higher than that of Ru/NC. In particular, both the intrinsic activity ($j^{0,s}$) and mass activity ($j^{k,m}$) at 50 mV of Ru–$RuSb_2$/NC are higher than that of the majority of the precious metal-based HOR catalysts in previously published studies (Fig. 3d and Table S2†).

The stability of the heterostructure has also been evaluated through the accelerated degradation test.[33] Considering the exact crystalline structure and specific atomic composition, the intermetallic compounds have been recognized as the catalysts with excellent stability. As shown in Fig. S9 and S10,† $RuSb_2$/NC

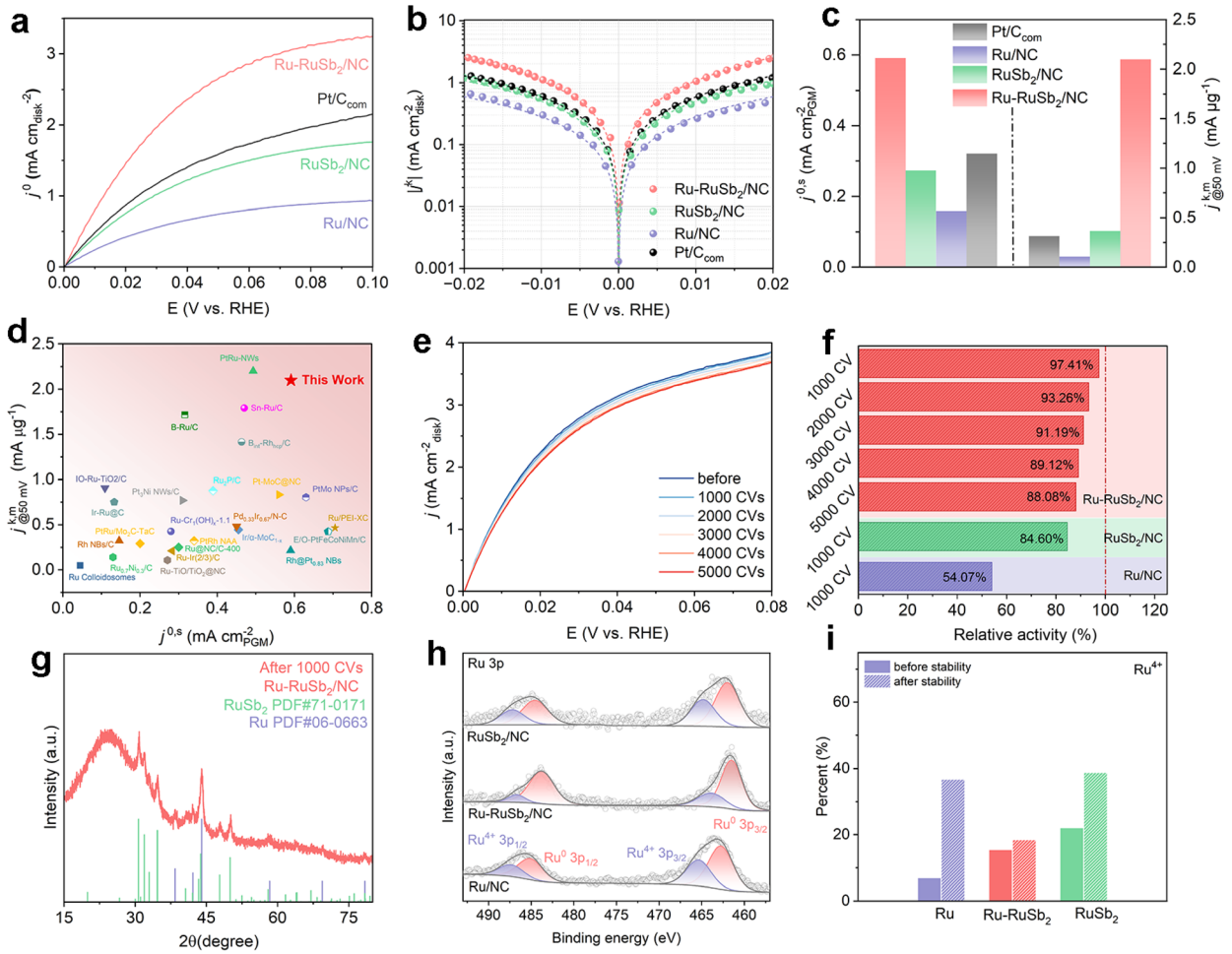

Fig. 3 (a) The HOR curves of Ru/NC, Ru–$RuSb_2$/NC, $RuSb_2$/NC and Pt/C_{com} at a rotating speed of 1600 rpm with a scan rate of 10 mV s^{-1} in H_2-saturated 0.1 M KOH. (b) Tafel plots with the Butler–Volmer fitting lines of Ru/NC, Ru–$RuSb_2$/NC, $RuSb_2$/NC and Pt/C_{com}. (c) Comparison of the intrinsic activities ($j^{0,s}$) and the mass activities ($j^{k,m}$) (at 50 mV) of Ru/NC, Ru–$RuSb_2$/NC, $RuSb_2$/NC and Pt/C_{com}. (d) Comparison of $j^{k,m}$ and $j^{0,s}$ of Ru–$RuSb_2$/NC with those of noble metal-based electrocatalysts reported in the literature. Details are summarized in Table S2.† (e) Polarization curves of Ru–$RuSb_2$/NC in H_2-saturated 0.1 M KOH at a rotating speed of 1600 rpm before and after 1000 CV, 2000 CV, 3000 CV, 4000 CV and 5000 CV cycles. (f) Comparison of the exchange current density (j^0) of Ru/NC, Ru–$RuSb_2$/NC and $RuSb_2$/NC after the stability test. (g) The XRD pattern of Ru–$RuSb_2$/NC after the stability test. (h) The Ru 3p XPS spectra of Ru/NC, Ru–$RuSb_2$/NC and $RuSb_2$/NC after the stability test. (i) The corresponding ratios of Ru^{4+} in Ru/NC, Ru–$RuSb_2$/NC and $RuSb_2$/NC before and after the stability test.

retained 84.06% exchange current density (j^0) after 1000 CV cycles, which is apparently higher than that of Ru/NC (54.07%). With the construction of the heterostructure, Ru–$RuSb_2$/NC only shows 2.59% attenuation of exchange current density (j^0) after 1000 CV cycles, which far exceeds that of $RuSb_2$/NC and Ru/NC (Fig. 3e and f). When increasing the number of cycles, Ru–$RuSb_2$/NC can still retain the HOR performance of 93.26%, 91.19% and 89.12% after 2000 CV, 3000 CV and 4000 CV cycles, respectively. When reaching 5000 CV cycles, Ru–$RuSb_2$/NC only declines to 11.92% exchange current density (j^0), which is still superior to that of $RuSb_2$/NC after 1000 CV cycles. The corresponding characterization after 1000 CV cycles was also performed to assess the stability. As shown in Fig. 3g, it is still clear that there are two phases in Ru–$RuSb_2$/NC, implying the good maintenance of the heterostructure. As shown in Fig. S11,† the XRD of $RuSb_2$/NC after the stability test was maintained well with before. In Fig. S12,† the crystallinity degree of Ru after the stability test apparently decreased, in line with the relatively inferior stability. The morphology and the corresponding nanoparticle size of Ru–$RuSb_2$/NC after the 1000 CV cycles are both same as before, further confirming excellent stability (Fig. S13†). Considering that the loss of HOR performance on Ru may originate from the oxidation on itself, the chemical state of Ru in all the catalysts after the stability test is depicted in Fig. 3h for comparison. The content of the oxidized Ru species in Ru/NC apparently enhanced compared with before, in line with the largely decreased activity after the stability test. In $RuSb_2$/NC, less amount of Ru has been oxidized, guaranteeing the higher stability than Ru/NC.[8] Furthermore, the oxidized Ru species in Ru–$RuSb_2$/NC just increase with a small proportion, indicating the excellent anti-oxidation ability of Ru on the heterostructure and contributing to the perfect stability (Fig. 3i). However, the oxidized Sb species in Ru–$RuSb_2$/NC after the stability test apparently increased compared with that of Ru

species, implying that the OH species in the heterostructure prefer to adsorb on Sb sites (Fig. S14†). The much higher oxidation degree of Sb than Ru after the stability test was observed in $RuSb_2$/NC, suggesting that the Sb can be the active site to adsorb OH species (Fig. S15†). The electron interaction and the enhanced d–p orbital coupling in the heterostructure contribute to the anti-oxidation ability of Sb in Ru–$RuSb_2$/NC.[34–36] Lower transition of oxidized Sb is demonstrated in Ru–$RuSb_2$/NC than that in $RuSb_2$/NC, which also facilitates the enhancement of the stability.

To investigate the mechanism of Ru–$RuSb_2$/NC on the improved HOR activity and stability, ultraviolet photoelectron spectroscopy (UPS) measurement was employed for the evaluation of the work function.[26] As shown in Fig. 4a, $RuSb_2$/NC depicts a higher work function (4.88 eV) than Ru/NC (4.73 eV). Due to the difference in work function between the two different crystal structures, a built-in electric field (BEF) was formed at the heterointerface in Ru–$RuSb_2$/NC (Fig. 4b), leading to the electron transfer from Ru to $RuSb_2$.[37,38] Thereby, the obtained Ru–$RuSb_2$/NC achieves a moderate work function compared with Ru/NC and $RuSb_2$/NC (Fig. S16†). Considering the electron redistribution on the surface of the heterostructure, the adsorption energy of OH species also changed on Ru–$RuSb_2$/NC. The CO stripping experiments of Ru/NC, Ru–$RuSb_2$/NC and $RuSb_2$/NC are shown in Fig. 4c to explore the OH adsorption behavior.[39] The apparently lower-shifted CO-stripping peak of Ru–$RuSb_2$/NC compared with that of Ru/NC and $RuSb_2$/NC indicates the enhanced OH binding energy on the surface, promoting the HOR performance of the heterostructure.

For comprehensively understanding the excellent HOR performance on the Ru–$RuSb_2$/NC heterostructure, *in situ* surface-enhanced infrared absorption spectroscopy (SEIRAS) was performed to explore the change in the interfacial water structure. In Fig. 4d, e and S17,† the O–H stretching mode of the interfacial water ranging from 3000 to 3600 cm^{-1} can be deconvoluted into three groups of peaks. The water molecules located in the gap region with vibration frequency around 3600 cm^{-1} are denoted as $H_2O_{(gap)}$, the water molecules above the gap region with vibration frequency around 3400 cm^{-1} are denoted as $H_2O_{(above\ gap)}$ and the water molecules near to the

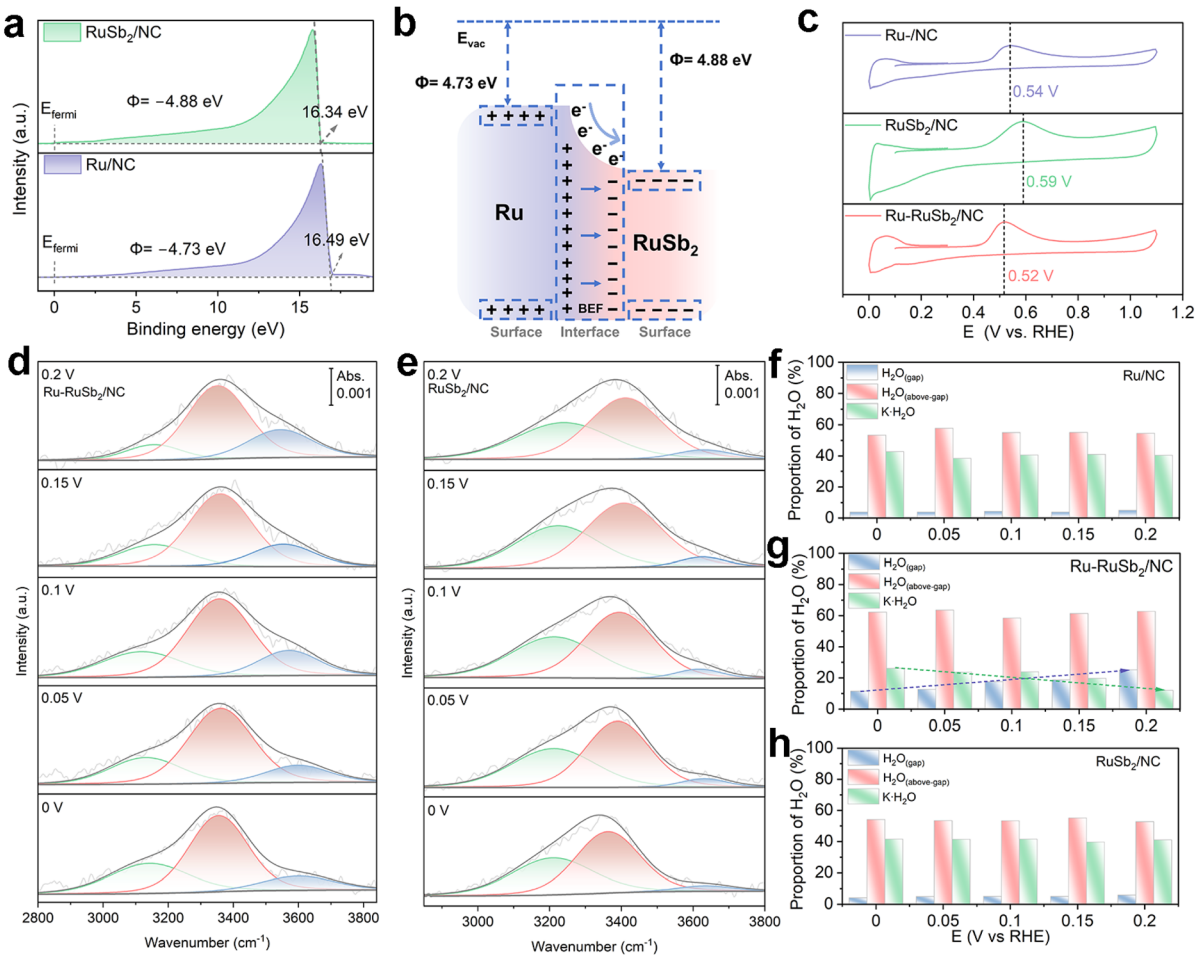

Fig. 4 (a) UPS spectra of $RuSb_2$/NC and Ru/NC. (b) Charge transfer process in Ru–$RuSb_2$. (c) CO stripping curves in CO-saturated 0.1 M KOH of Ru/NC, Ru–$RuSb_2$/NC and $RuSb_2$/NC. Deconvolution of the O–H stretching vibration features of *in situ* SEIRAS spectra recorded at potentials from 0 V to 0.2 V *vs.* RHE for Ru–$RuSb_2$/NC (d) and $RuSb_2$/NC (e) in 0.1 M KOH. The proportion of the three kinds of water molecules from the deconvolution of the O–H stretching vibration features of Ru/NC (f), Ru–$RuSb_2$/NC (g) and $RuSb_2$/NC (h).

electrode surface with vibration frequency around 3200 cm^{-1} are denoted as $K{\cdot}H_2O$.[17] As shown in Fig. 4f–h, it is clear that the proportion of $H_2O_{(gap)}$ on Ru–$RuSb_2$/NC is apparently higher than that on Ru/NC and $RuSb_2$/NC at all the potentials and the proportion of $H_2O_{(gap)}$ also enhances with the increase of the potential on the surface of Ru–$RuSb_2$/NC, which reveals the enhancement of the water concentration in the gap zone in Ru–$RuSb_2$/NC EDL and the improvement of the connectivity of the hydrogen bonding network. It is also worth noting that the proportion of $K{\cdot}H_2O$ on Ru–$RuSb_2$/NC is lower than that on Ru/NC and $RuSb_2$/NC and its proportion decreases as the potential is enhanced, which is in agreement with the increased proportion of $H_2O_{(gap)}$. Considering the enhanced OH adsorption on the heterostructure, more OH species on the surface of Ru–$RuSb_2$/NC can coordinate with K^+, leading to breaking of the solvation sheath on $K{\cdot}H_2O$ and providing more $H_2O_{(gap)}$ to the gap zone.[17,40] Thus, it improves the connectivity of the hydrogen bonding network and accelerates the transfer of protons, thereby accelerating the water formation step on Ru–$RuSb_2$/NC and improving the HOR performance. Besides, the difference in the O–H stretching wavenumbers between $H_2O_{(above\ gap)}$ and $H_2O_{(gap)}$ on Ru–$RuSb_2$/NC is lower than that on Ru/NC and $RuSb_2$/NC, which further indicates the promotion of the connectivity of hydrogen bonding network and helps in the transfer of protons (Fig. S18†). The *in situ* SEIRAS spectra of Ru–$RuSb_2$/NC after the stability test are also captured in Fig. S19 and S20† for evaluating the origin of the excellent stability. The proportion of the three kinds of water is still the same as before, indicating the maintenance of the high connectivity of the hydrogen bonding network on Ru–$RuSb_2$/NC. The resulting rapid HOR process of the catalysts during the stability test also can speed up the transformation of OH, relieving the attack of OH on Ru and further elevating the stability of Ru–$RuSb_2$/NC.[19]

For further investigation of the electron redistribution and the adsorption behavior of the intermediate during the HOR process, density functional theory (DFT) calculations were employed. In Fig. 5a and b, the work functions of Ru and $RuSb_2$ are calculated to be 4.47 eV and 4.60 eV, respectively. The difference in the work function of these two catalysts is in line with the order of the UPS results, implying the electron transfer between the Ru and $RuSb_2$ with the BEF.[41,42] In addition, the electron localization function (ELF) in Fig. S21† verifies the existence of the chemical bonds of Ru–Ru and Ru–Sb between Ru and $RuSb_2$ in the heterostructure.[26,43] With the formation of the interface-induced chemical bonding, the charge localized redistribution is promoted, benefiting the electron transfer at the interface. The differential charge density depicted in Fig. 5c further supports this view with the 9.63 electron transfer from Ru to $RuSb_2$. Considering the electron redistribution, the work function of Ru–$RuSb_2$ is also modified to a moderate level (Fig. S22†), which conforms to the result of UPS. The d-band center of Ru–$RuSb_2$ is affected owing to the charge transfer at the interface. In Fig. S23,† the d band center of Ru in the catalysts gradually moves away from the Fermi level (E_f) with the enhancement of the electron loss in the order of Ru, Ru–$RuSb_2$ and $RuSb_2$. With the increased antibonding orbitals occupied in Ru, the OH adsorption energy on the Ru sites of $RuSb_2$ and Ru–

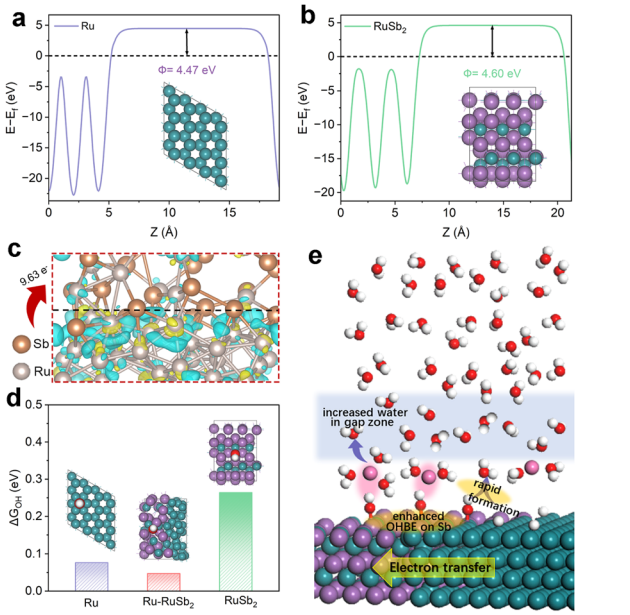

Fig. 5 The electrostatic potential profiles of Ru (a) and $RuSb_2$ (b) surfaces with the corresponding structure models (insets). (c) Differential charge density for the Ru–$RuSb_2$ interface. (d) The adsorption energy of OH on Ru, Ru–$RuSb_2$ and $RuSb_2$ with the corresponding optimal theoretical structures (insets). (e) Schematic illustration of the change in the interfacial water structure on the heterostructure. The purple balls represent Sb atoms, green balls represent Ru atoms, red balls represent O atoms, white balls represent H atoms and pink balls represent K^+.

$RuSb_2$ apparently decreased (Fig. S24 and S25†).[44] With the injection of the electron from Ru, Sb becomes the new active site on $RuSb_2$ and Ru–$RuSb_2$, which shows the strengthened OH binding energy compared with that on the Ru site (Fig. 5d) and in line with the results of XPS. With the higher orbital coupling state diagram of the O adsorption state on Sb (Fig. S26†), Ru–$RuSb_2$ presents a higher OH binding energy than that of $RuSb_2$, which is also stronger than that of Ru (Fig. 5d) and in line with the results of CO STP. The stronger OH adsorption on Sb sites of Ru–$RuSb_2$ largely diminish the OH attack on Ru, preventing the oxidation of Ru, thereby elevating the stability of the heterostructure. It also elevates the connectivity of the hydrogen bonding network as mentioned above. Besides, the hydrogen binding energy on the three samples is also investigated. According to the lower shift of the d-band center, the adsorption of H on $RuSb_2$ and Ru–$RuSb_2$ declines compared with that on Ru (Fig. S27 and S28†). In particular, the hydrogen adsorption free energy (ΔG_{H^*}) on the heterostructure is closest to the ideal value of 0 eV, which also guarantees the perfect HOR activity on Ru–$RuSb_2$.[45] In addition, the reaction paths of Ru, Ru–$RuSb_2$ and $RuSb_2$ are calculated in Fig. S29–S32.† Ru–$RuSb_2$ depicts the lowest energy barrier of water desorption compared to Ru and $RuSb_2$, which can further speed up the HOR process. Along with the results of the DFT calculation and *in situ* SEIRAS, the adsorption behavior of the intermediate and the interfacial water structure can be concluded as in Fig. 5e.

Conclusions

In conclusion, the Ru–$RuSb_2$/NC heterostructure has been successfully synthesized with excellent HOR performance and stability. Due to the difference in work function between Ru and $RuSb_2$, the formed BEF at the interface leads to charge transfer from Ru to $RuSb_2$, which further enhances the OH adsorption on the Ru–$RuSb_2$/NC heterostructure. According to the *in situ* SEIRAS investigation and theoretical calculations, the optimized OH adsorption on the surface improves the connectivity of the hydrogen bonding network and speeds up the transfer of protons, promoting the water formation step. As a result, the mass activity ($j^{k,m}$) of Ru–$RuSb_2$/NC reaches 2.098 mA μg^{-1} at 50 mV, which is 6-fold and 20-fold higher than that of Pt/C_{com} and Ru/NC, respectively. Owing to the enhanced OH adsorption on Sb sites and the fast reaction process originating from the connected hydrogen bonding network, the Ru in Ru–$RuSb_2$/NC presents elevated anti-oxidation ability, which contributes to the enhanced stability with 2.59% activity decay after 1000 CV cycles. This work sheds new light on constructing intermetallic catalysts for alkaline HOR and provides a distinctive method for improving the stability of Ru-based catalysts towards alkaline HOR.

Data availability

The data supporting this article have been included as part of the ESI.†

Author contributions

CY, ZD, JY performed the material synthesis and electrochemical tests. ZD performed the DFT calculations. WL supervised the work. CY and WL wrote the manuscript.

Conflicts of interest

There are no conflicts to declare.

Acknowledgements

This work was financially supported by the National Natural Science Foundation of China (22272121). We thank the Core facility of Wuhan University for the ICP-AES and XPS measurements and the Core Research Facilities of College of Chemistry and Molecular Sciences for the TEM and XRD measurements. The authors would like to acknowledge the Center for Electron Microscopy at Wuhan University for their substantial support to JEM-ARM200F and the supercomputing system in the Supercomputing Center of Wuhan University for DFT calculations. We thank theShanghai Synchrotron Radiation Facility of BL14B1 (**https://cstr.cn/31124.02.SSRF.BL11B**) for assistance in measurements.

Notes and references

1 G. Glenk and S. Reichelstein, *Nat. Energy*, 2019, **4**, 216–222.
2 I. Staffell, D. Scamman, A. Velazquez Abad, P. Balcombe, P. E. Dodds, P. Ekins, N. Shah and K. R. Ward, *Energy Environ. Sci.*, 2019, **12**, 463–491.
3 X. Song, Q. Yang, K. Zou, Z. Xie, J. Wang and W. Ding, *Adv. Funct. Mater.*, 2025, **35**, 2414570.
4 J. Huang, L. Sementa, Z. Liu, G. Barcaro, M. Feng, E. Liu, L. Jiao, M. Xu, D. Leshchev, S.-J. Lee, M. Li, C. Wan, E. Zhu, Y. Liu, B. Peng, X. Duan, W. A. Goddard, A. Fortunelli, Q. Jia and Y. Huang, *Nat. Catal.*, 2022, **5**, 513–523.
5 X. Wang, Z. Li, Y. Qu, T. Yuan, W. Wang, Y. Wu and Y. Li, *Chem*, 2019, **5**, 1486–1511.
6 F. Xiao, Y.-C. Wang, Z.-P. Wu, G. Chen, F. Yang, S. Zhu, K. Siddharth, Z. Kong, A. Lu, J.-C. Li, C.-J. Zhong, Z.-Y. Zhou and M. Shao, *Adv. Mater.*, 2021, **33**, 2006292.
7 R. K. Singh, E. S. Davydova, J. Douglin, A. O. Godoy, H. Tan, M. Bellini, B. J. Allen, J. Jankovic, H. A. Miller, A. C. Alba-Rubio and D. R. Dekel, *Adv. Funct. Mater.*, 2020, **30**, 2002087.
8 F. Yang, Y. Wang, Y. Cui, X. Yang, Y. Zhu, C. M. Weiss, M. Li, G. Chen, Y. Yan, M. D. Gu and M. Shao, *J. Am. Chem. Soc.*, 2023, **145**, 27500–27511.
9 J. Wu, X. Gao, G. Liu, X. Qiu, Q. Xia, X. Wang, W. Zhu, T. He, Y. Zhou, K. Feng, J. Wang, H. Huang, Y. Liu, M. Shao, Z. Kang and X. Zhang, *J. Am. Chem. Soc.*, 2024, **146**, 20323–20332.
10 L. Wei, W. Yan, Z. Huang, R. Li, Q. Kong, W. Huang, C. Pao, Z. Hu, H. Lin, N. Chen, Y. Xu, H. Geng and X. Huang, *Energy Environ. Sci.*, 2024, **17**, 5922–5930.
11 Y. Cong, H. Wang, M. Liu and J. Tian, *Appl. Catal., A*, 2024, **676**, 119684.
12 L. Li, S. Liu, C. Zhan, Y. Wen, Z. Sun, J. Han, T.-S. Chan, Q. Zhang, Z. Hu and X. Huang, *Energy Environ. Sci.*, 2023, **16**, 157–166.
13 Y. Cong, C. Chai, X. Zhao, B. Yi and Y. Song, *Adv. Mater. Interfaces*, 2020, **7**, 2000310.
14 Y. Cui, Z. Xu, D. Chen, T. Li, H. Yang, X. Mu, X. Gu, H. Zhou, S. Liu and S. Mu, *Nano Energy*, 2021, **90**, 106579.
15 J. Durst, A. Siebel, C. Simon, F. Hasché, J. Herranz and H. A. Gasteiger, *Energy Environ. Sci.*, 2014, **7**, 2255–2260.
16 W. Chen, M. Yu, S. Liu, C. Zhang, S. Jiang and G. Duan, *Adv. Funct. Mater.*, 2024, **34**, 2313307.
17 P. Li, Y. Jiang, Y. Hu, Y. Men, Y. Liu, W. Cai and S. Chen, *Nat. Catal.*, 2022, **5**, 900–911.
18 T. Takeguchi, T. Yamanaka, K. Asakura, E. N. Muhamad, K. Uosaki and W. Ueda, *J. Am. Chem. Soc.*, 2012, **134**, 14508–14512.
19 Y. Fang, C. Wei, Z. Bian, X. Yin, B. Liu, Z. Liu, P. Chi, J. Xiao, W. Song, S. Niu, C. Tang, J. Liu, X. Ge, T. Xu and G. Wang, *Nat. Commun.*, 2024, **15**, 1614.
20 L. Wei, Y. Dong, W. Yan, Y. Zhang, C. Zhan, W.-H. Huang, C.-W. Pao, Z. Hu, H. Lin, Y. Xu, H. Geng and X. Huang, *Angew. Chem., Int. Ed.*, 2025, **64**, e202420177.
21 K. Deng, J. Yu, Q. Mao, R. Yang, H. Yu, Z. Wang, J. Wang, L. Wang and H. Wang, *Adv. Funct. Mater.*, 2025, 2420728.
22 X. Ke, Y. Yang, F. Zhou, Y. Chen, M. Zhao, Q. Xu, N. Liu, C. Zou, H. Jin, L. Zhang and S. Wang, *Chem. Eng. J.*, 2023, **476**, 146815.

23 Y. Zhang, G. Li, Z. Zhao, L. Han, Y. Feng, S. Liu, B. Xu, H. Liao, G. Lu, H. L. Xin and X. Huang, *Adv. Mater.*, 2021, **33**, 2105049.
24 Z. Huang, S. Hu, M. Sun, Y. Xu, S. Liu, R. Ren, L. Zhuang, T. Chan, Z. Hu, T. Ding, J. Zhou, L. Liu, M. Wang, Y. Huang, N. Tian, L. Bu, B. Huang and X. Huang, *Nat. Commun.*, 2024, **15**, 1097.
25 S. Zhu, Z. Li, L. Hou, M. G. Kim, H. Jang, S. Liu and X. Liu, *Adv. Funct. Mater.*, 2024, **34**, 2314899.
26 J. Park, H. Kim, S. Kim, S. Y. Yi, H. Min, D. Choi, S. Lee, J. Kim and J. Lee, *Adv. Mater.*, 2024, **36**, 2308899.
27 L. Hou, Z. Li, H. Jang, M. G. Kim, J. Cho, W. Zhong, S. Liu and X. Liu, *Angew. Chem., Int. Ed.*, 2025, **64**, e202423756.
28 D. Chen, R. Lu, R. Yu, Y. Dai, H. Zhao, D. Wu, P. Wang, J. Zhu, Z. Pu, L. Chen, J. Yu and S. Mu, *Angew. Chem., Int. Ed.*, 2022, **61**, e202208642.
29 X. Huang, J. Feng, S. Hu, B. Xu, M. Hao, X. Liu, Y. Wen, D. Su, Y. Ji, Y. Li, Y. Li, Y. Huang, T.-S. Chan, Z. Hu, N. Tian, Q. Shao and X. Huang, *Nat. Nanotechnol.*, 2024, **19**, 1306–1315.
30 X. Tian, P. Zhao and W. Sheng, *Adv. Mater.*, 2019, **31**, 1808066.
31 Y. Cong, B. Yi and Y. Song, *Nano Energy*, 2018, **44**, 288–303.
32 C. L. Green and A. Kucernak, *J. Phys. Chem. B*, 2002, **106**, 1036–1047.
33 H. Xie, S. Chen, J. Liang, T. Wang, Z. Hou, H.-L. Wang, G. Chai and Q. Li, *Adv. Funct. Mater.*, 2021, **31**, 2100883.
34 W. Xiao, W. Lei, M. Gong, H. Lin and D. Wang, *ACS Catal.*, 2018, **8**, 3237–3256.
35 L. Gao, X. Lin, Z. Yao, H. Bai, Y. Lu, C. Ma, S. Lu, Z. Peng, J. Yang, A. Pan and H. Huang, *J. Am. Chem. Soc.*, 2019, **141**, 18083–18090.
36 X. Ai, X. Zou, H. Chen, Y. Su, X. Feng, Q. Li, Y. Liu, Y. Zhang and X. Zou, *Angew. Chem., Int. Ed.*, 2020, **59**, 3961–3965.
37 Z. Chen, H. Qing, R. Wang and R. Wu, *Energy Environ. Sci.*, 2021, **14**, 3160–3173.
38 J. Jing, J. Yang, Z. Zhang and Y. Zhu, *Adv. Energy Mater.*, 2021, **11**, 2101392.
39 L.-F. Shen, B.-A. Lu, X.-M. Qu, J.-Y. Ye, J.-M. Zhang, S.-H. Yin, Q.-H. Wu, R.-X. Wang, S.-Y. Shen, T. Sheng, Y.-X. Jiang and S.-G. Sun, *Nano Energy*, 2019, **62**, 601–609.
40 Y.-H. Wang, Y. Yang, F.-Y. Gao, X.-L. Zhang, L. Zhu, H.-K. Yan, P.-P. Yang and M.-R. Gao, *Angew. Chem., Int. Ed.*, 2024, **63**, e202407613.
41 L. Zhai, X. She, L. Zhuang, Y. Li, R. Ding, X. Guo, Y. Zhang, Y. Zhu, K. Xu, H. J. Fan and S. P. Lau, *Angew. Chem., Int. Ed.*, 2022, **61**, e202116057.
42 Z. Yuan, J. Li, M. Yang, Z. Fang, J. Jian, D. Yu, X. Chen and L. Dai, *J. Am. Chem. Soc.*, 2019, **141**, 4972–4979.
43 Z. Luo, L. Zhang, L. Wu, L. Wang, Q. Zhang, X. Ren and X. Sun, *Nano Energy*, 2022, **102**, 107654.
44 B. Hammer, O. H. Nielsen and J. K. Nrskov, *Catal. Lett.*, 1997, **46**, 31–35.
45 J. Deng, H. Li, S. Wang, D. Ding, M. Chen, C. Liu, Z. Tian, K. S. Novoselov, C. Ma, D. Deng and X. Bao, *Nat. Commun.*, 2017, **8**, 14430.